Anion Resonances and Photoelectron Spectroscopy of the Tetracenyl Anion

Cole R. Sagan, and Etienne Garand*

Department of Chemistry, University of Wisconsin-Madison, 1101 University Avenue, Madison, WI 53706, United States

*Author to whom correspondence should be addressed.

email: egarand@wisc.edu

Abstract

The photoelectron spectroscopy of the tetracenyl anion using slow electron velocity-map imaging (SEVI) of cryogenically cooled ions is presented. The total photodetachment yield as a function of photon energy is used to reveal a rich manifold of anion excited states above the detachment threshold. The lowest energy anionic resonance has a sufficiently long lifetime to yield a vibrationally resolved absorption spectrum that can be directly compared with theoretical predictions. Excitation of this state mostly results in electron detachment via thermionic emission. The total photodetachment yield spectrum is used to select photon wavelengths that minimize the indirect detachment signal to allow acquisition of vibrationally-resolved photoelectron spectra that can inform on the neutral tetracenyl radical. Assignment of spectral features corresponding to the ground and first excited state of the neutral 12-tetracenyl isomer is made with the aid of Franck-Condon simulations. This yields adiabatic electron affinity and term energies that differ significantly from the previously reported values. Weak features corresponding to the ground state of the minor 2-teracenyl and 1-tetracenyl isomers are also identified, which allows for the experimental determination of their electron affinities for the first time.

I. Introduction

Polycyclic aromatic hydrocarbons (PAHs), and their unique properties due to their large conjugated π-orbital systems, have been the subject of many studies for their roles in different chemistry fields. In particular, PAHs are thought to be the most ubiquitous complex molecules in space,[1,2] where they can exist in their hydrogenated, dehydrogenated or protonated forms.[1,3] Given their abundances, adoption of multiple different forms, and strong absorption features, PAHs are suspected to be major contributors to diffuse interstellar bands.[4] The formation of larger PAHs is also hypothesized to occur through reactions with smaller dehydrogenated PAH radicals.[5,6] PAH anions, formed via radiative electron attachment or dissociative electron attachment to the corresponding neutral PAHs, can also play a role in the chemistry of dense molecular clouds.[7–10] In this paper, we report the study of the dehydrogenated tetracenyl ($C_{18}H_{11}$) anion and neutral radical using both high-resolution photoelectron spectroscopy and total photodetachment yield spectroscopy.

Anion photoelectron spectroscopy, in which the kinetic energy of the photoelectron ejected from the closed-shell deprotonated anion is measured, is well-suited for studying the corresponding radical neutral dehydrogenated PAHs. When sufficient resolution is achieved using slow photoelectron velocity-map imaging (SEVI)[11,12] of cryogenically cooled ions,[13–16] it can provide detailed insights into the ground and excited states of the neutral radical. This approach has been used by Neumark and co-workers[17,18] to study the naphthyl ($C_{10}H_7$) and anthracenyl ($C_{14}H_9$) radical species. The next largest dehydrogenated PAH, tetracenyl ($C_{18}H_{11}$), has been studied by Verlet and co-workers[19] using anion photoelectron spectroscopy. However, for tetracenyl, the spectra showed strong interference from thermionic emission, an indirect electron detachment process. This suggested the presence of anion excited states above the detachment

threshold that were resonantly excited by the photodetachment laser. Such anion excited states, which are related to the transient resonances observed in electron loss spectroscopy,[20–22] have also been observed in the related anthracenyl anion[23] and other similar PAHs.[24–29]

Here, we revisit the photoelectron spectroscopy of the tetracenyl anion using SEVI of cryogenically cooled ions. We start with the measurement of the total photodetachment yield as a function of photon energy, which reveals a rich manifold of anion excited states above the detachment threshold. Interestingly, the lowest energy of these states has features with narrow linewidth, which yields a vibrationally resolved absorption spectrum that can be directly compared with theoretical predictions. Resonant excitation of these anionic states mostly results in electron detachment via thermionic emission that often completely obscure the direct detachment signal. Careful wavelength selection is thus used to minimize the intensity of the indirect detachment signal and acquire vibrationally-resolved photoelectron spectra that can inform on the neutral tetracenyl radical. Aided by Franck-Condon simulations, the main features observed in the photoelectron spectra are assigned to the ground and first excited state of the neutral 12-tetracenyl isomer. This yields adiabatic electron affinity and term energies which are significantly different than the previously reported values.[19] Weak features corresponding to the ground state of the minor 2-teracenyl and 1-tetracenyl isomers are also identified, which allows for the experimental determination of their electron affinities for the first time.

II. Experimental and Theoretical methods

The total photodetachment and anion photoelectron spectra were obtained using our cryogenic SEVI instrument described in detail previously.[30] The tetracenyl anions were generated

by electron impact inside a room-temperature linear octupole ion trap. Briefly, tetracene powder was placed inside a small reservoir located near the side of the ion trap, and the reservoir was heated to 110 °C using a Peltier module. A gas mixture composed of 1% CH_4 in a balance of helium flowed over the reservoir and picked up tetracene vapor. The mixture then flowed into the internal volume of the ion trap via a short tube. The gas flow was adjusted using a mass flow controller to maintain a 10 mtorr pressure in the vacuum chamber. Anions were generated directly inside the ion trap by ~180 eV electrons produced by a thoriated (1%) tungsten filament located outside of one of the axial apertures of the ion trap.

The room-temperature anions thus formed were extracted from the linear octupole trap and transferred into a cryogenic 3-D quadrupole ion trap. The 3-D ion trap, located in a separate differentially pumped vacuum region, was held at 10 K by a closed-cycle helium cryocooler. A short pulse of helium buffer gas was introduced into the ion trap to collisionally cool the internal temperature of the anions. After a delay of ~95 ms to allow for the evacuation of the buffer gas from the trap volume, the cooled anions were ejected into a time-of-flight mass spectrometer for mass separation. A pulsed re-referencing voltage in front of the multi-plates velocity-map imaging (VMI) region mass-selected for only the tetracenyl anions. In the VMI region, the ion packet was intersected by the output of a tunable 10 Hz Nd:YAG pumped UV/Vis optical parametric oscillator (OPO) with a 5–7 cm^{-1} linewidth. The generated photoelectrons were focused onto a pair of 40 mm MCP detectors coupled to a phosphor screen. The resulting photoelectron images were captured by a 2048 × 2048 CMOS camera.

The raw images were circularized[31], quadrant symmetrized, inverse Abel transformed,[32] and radially integrated to obtain the photoelectron spectra. The electron kinetic energies were calibrated using the known photoelectron features of I^-. For easier comparisons between

photoelectron spectra acquired using different photon energies, the spectra are plotted as a function of electron binding energy (eBE), which is the difference between the photon energy and the measured kinetic energy of the photoelectrons.

The total photodetachment yield spectra were collected by stepping the laser wavelength in 0.1nm increments. At each wavelength, the total number of photoelectrons per laser shot was counted, and averaged for a total of 15 laser shots. The total photodetachment yield spectra are then generated by plotting the photoelectron count, normalized to the photon flux, as a function of photon energy.

Density functional theory (DFT) were carried out with the B3LYP functional and the def2-TZVP basis set augmented with diffuse functions (def2TZVPD),[33,34] using the Gaussian 16 program.[35] This functional has been used with success to describe the tetracenyl anion and radical previously.[36] All the reported energies here include zero-point energy correction from the unscaled harmonic frequencies. The Franck-Condon simulations were calculated using the ezSpectrum program[37] and include Duschinsky rotations.

III. Results

a) Computational results

Three tetracenyl isomers are possible, 1-tetracenyl, 2-tetracenyl and 12-tetracenyl, depending on which H is removed from tetracene. Their structures are shown in Figure 1. For the neutral doublet ground state ($\tilde{X}^2A'$), the 1-Tet and 2-Tet isomers are calculated to be nearly isoenergetic and ~140 cm^{-1} (~1.7 kJ/mol) lower than the 12-Tet isomer. The situation is different for the anion singlet ground-state ($\tilde{X}^1A'$), where the 12-Tet isomer is calculated to be 1440 cm^{-1}

(17.3 kJ/mol) and 1760 cm^{-1} (21.1 kJ/mol) below the 1-Tet and 2-Tet isomers, respectively. This yields a predicted adiabatic electron affinity (AEA) of 14250 cm^{-1} (1.77 eV) for 12-Tet, which is higher than the 12678 cm^{-1} (1.57 eV) and 12347 cm^{-1} (1.53 eV) AEA predicted for 1-Tet and 2-Tet, respectively. All three predicted AEAs are significantly lower than the 2.4 eV experimental value reported by Verlet and co-workers.[19] However, they are consistent with some previous DFT studies.[36] All three tetracenyl isomers exhibit similar geometry changes between the anion and neutral ground states, which are mostly located at the hydrogen atom removal site. Notably, the C-C-C bond angle ($\theta_{C\text{-}C\text{-}C}$ indicated in Figure 1) changes from ~113° in the anion ground-state to ~127° in the neutral ground-state, consistent with previous DFT studies.[36]

The lowest-energy neutral excited state corresponds to the promotion of an π electron into the singly occupied (SOMO) σ orbital at the hydrogen removal site. In the C_s symmetry, this excitation results in a $\tilde{A}^2A''$ state. DFT predicts this $^2A''$ state to be a saddle-point with an imaginary frequency corresponding to an out-of-plane vibration, and an adiabatic term energy of ~7750 cm^{-1} (0.96 eV) for the 12-Tet isomer. Similar saddle points were found with adiabatic term energies of ~9700 cm^{-1} and ~11000 cm^{-1} for 1-Tet and 2-Tet, respectively. Unfortunately, it was not possible to converge the computations on the lower symmetry structures.

Several low-lying valence excited states are predicted on the anion surface by the DFT calculations. The lowest energy one corresponds to a $\sigma \rightarrow \pi$ transition involving the promotion of an σ electron from the orbital at the hydrogen removal site (HOMO) to the lowest-energy unoccupied π orbital (LUMO). Fortenberry and co-workers calculated a vertical excitation energies of 1.99 eV for this anionic state in 12-Tet using equation-of-motion coupled-cluster (EOM-CCSD),[38] which is somewhat larger than the 1.14 eV found here with DFT. Geometry optimization of this $\tilde{A}^1A''$ state in the C_s symmetry lead to a saddle point situated less than 0.25 eV

above the ground state. Therefore, DFT predicts this anion excited state to be a bound state, i.e., below the electron detachment threshold. However, its low oscillator strength (f = 0.0001) and low term energy means that it is unlikely to interfere with the direct photodetachment process. The second excited state is a $\pi \rightarrow \pi$ transition involving the promotion of an electron from the HOMO-1 to the LUMO. This excited-state ($\tilde{B}^1A'$) is a minimum in the C_s symmetry with a calculated adiabatic excitation energy of 15350 cm^{-1} (1.90 eV) and an oscillator strength of f = 0.0301 for the 12-Tet isomer. The optimized geometry is close to that of the ground anion state, with $\theta_{C\text{-}C\text{-}C}$ = 114.9°. Slightly smaller adiabatic term energies of 13160 cm^{-1} (1.63 eV) and 13590 cm^{-1} (1.69 eV) were found for the corresponding excited state in the 1-Tet and 2-Tet isomers. This anion excited state is thus predicted to be slightly above the detachment threshold but lies in the photon energy range used for acquiring direct photodetachment spectra.

b) Total photodetachment yield spectrum

The computational results presented above suggest the presence of several anion excited states above the detachment threshold that can be excited by the detachment laser. In order to potentially map these excited states and determine the best photon energy for minimizing interferences from indirect detachment, we acquired the total photodetachment yield spectrum in the 14000 - 29000 cm^{-1} region (Figure 2). The total photoelectron count starts increasing above 15000 cm^{-1}, but a small amount of photoelectrons can be produced below that threshold. Two small peaks are found at 16310 cm^{-1} and 16650 cm^{-1}. The total photodetachment yield then sharply rises just before 17000 cm^{-1} and a series of intense peaks are clearly resolved between 17000 - 19000 cm^{-1}. This non-monotonic increase in photodetachment yield is a clear signature of an anion

excited state whose resonant excitation followed by indirect detachment is producing a significant percentage of the observed photoelectrons. The most intense peaks between 17000 - 18000 cm^{-1} have regular spacings of about 170 cm^{-1} and 310 cm^{-1}, suggesting a vibrational Franck-Condon progression. These peaks also have FWHM of 30-50 cm^{-1}. This is much broader than what is expected from the ~5 cm^{-1} laser linewidth and a ~10 cm^{-1} unresolved rotational envelope. Above 19000 cm^{-1}, the total photodetachment yield generally decreases and individual vibrations are no longer resolvable. At higher energy, three additional intense and broad (~100-400 cm^{-1} FWHM) features are seen at ~ 25000 cm^{-1}, ~25900 cm^{-1} and ~26500 cm^{-1}.

To investigate the different processes involved in the generation of the photoelectrons, we acquired a series of SEVI images at different photon energies, indicated by arrows in Figure 2. These photoelectron spectra are shown in Figure 3. The spectra acquired with photon energies below 17000 cm^{-1} (λ_{3A}, λ_{3B}, and λ_{3C}) contain features with consistent position and intensity across different spectra. The major difference here involves features having lower intensities closer to threshold, which is expected from Wigner threshold law.[39] Therefore, these photoelectron spectra can be analyzed as resulting from regular direct photodetachment. We note that the photoelectron spectra acquired with photon energies λ_{3A} and λ_{3B}, which are resonant with weak features in Figure 2, exhibit small but noticeable differences in the intensity of features that are below 14800 cm^{-1} compared to λ_{3C}. This is highlighted by the insets in Figure 3A-C.

The photoelectron spectra obtained with photon energies resonant with some of the most intense peaks in Figure 2 have noticeably different appearance than those acquired at lower photon energies. The photoelectron spectrum in Figure 3D, taken at 16964 cm^{-1} (λ_{3D}), displays a very intense feature near zero eKE. A similar feature is found in Figure 3E spectrum, taken at 18090 cm^{-1} (λ_{3E}), and Figure 3F spectrum, acquired with 18450 cm^{-1} (λ_{3F}) photons. These two spectra

also show an intense and broad background signal extending from zero eKE to ~16000 cm^{-1}. Further analysis of the anion excited state and subsequent indirect detachment process is presented in section IVb.

c) Direct detachment spectra

The photoelectron spectra relevant to the analysis of the tetracenyl neutral ground state are shown in Figure 4. Spectra 4B and 4C were acquired with photon energies of 16815 cm^{-1} and 15998 cm^{-1}, below the onset of the anion excited $\tilde{B}^1A'$ state. Spectrum 4A was acquired with photon energy above that onset, at 17500 cm^{-1}, which is in between two peaks in Figure 2. Therefore, spectrum 4A contains some contributions from indirect detachment at very low eKE, but otherwise shows the same extended vibrational progressions consistent with direct detachment. The lowest energy peak observed, Peak X_A, is found at eBE = 14887 cm^{-1}. The main vibrational progression, formed by peaks X_A, X_D and X_L, has a spacing of ~600 cm^{-1}. The positions of the observed peaks X_A-X_N are listed in Table 1.

Because weak, but photon energy dependent, features were identified below eBE of 14800 cm^{-1} in Figure 3, we also acquired an additional photoelectron spectrum at 14747cm^{-1}. This spectrum, shown in Figure 5, displays numerous partially resolved peaks, labeled X_a-X_t, that extend down to eBE of 12480 cm^{-1}. It should be noted that the most intense features in Figure 5 are roughly 100 times weaker than peak X_A in Figure 4.

Finally, SEVI images were acquired at photon energy of 24610 cm^{-1} to locate the first neutral excited-state, and the photoelectron spectrum is shown in Figure 6. This photon energy is located at the onset of the intense photodetachment yield feature at 25000 cm^{-1} (λ_{6A} in Figure 2).

Therefore, the photoelectron spectrum contains significant amount of low eKE electrons (not shown in the figure) and a substantial background at all eKE. Nevertheless, a short series of peaks, labeled A_A-A_E, can clearly be resolved between 22500 - 23500 cm^{-1}. Peak A_A, the first and most intense peak of the series, is found at eBE of 22570 cm^{-1}. Because of the background intensities, higher resolution photoelectron spectra could not be acquired closer to the detachment threshold. The positions of the dominant observed features in Figure 6 are tabulated in Table 1.

IV. Analysis and discussion

a) Direct detachment spectra

We begin with the assignment of the direct photodetachment photoelectron spectra shown in Figure 4. The position of peak X_A at 14887 cm^{-1} is in best agreement with the 14250 cm^{-1} calculated origin transition of the 12-Tet isomer. The calculated Franck-Condon (FC) spectrum for the $\tilde{X}^2A' \leftarrow \tilde{X}^1A'$ transition of 12-Tet is shown in Figure 4D and it is found to be in overall excellent agreement with the experimental spectra shown in Figure 4A-C. The 1-Tet and 2-Tet isomers have lower predicted AEA and their calculated FC spectra (shown in Figure 5B-C) are not consistent with the positions and intensities of features X_A-X_N in Figure 4. Therefore, we assign features X_A-X_N to transitions to the neutral ground state of the dominant 12-Tet isomer.

This assignment is consistent with the calculated relative energy of the 12-Tet anion being 1400-1800 cm^{-1} lower than the other two isomers. This result suggests that, in our experiment, the anions are not formed by electron attachment to the neutral tetracenyl radical, in which all three isomers have similar energies. More likely, tetracenyl anions are formed by electron attachment to

tetracene followed by dissociation of a C-H bond.[40] This is certainly consistent with our experimental observations of intact tetracene anions under certain source conditions.

This assignment yields an electron affinity of 1.8457±0.0005 eV for the 12-Tet isomer. The assignment of individual spectral features is complicated by overlapping active vibrations in the calculated FC spectrum. Complete peak assignments are tabulated in Table 1. Overall, the FC active vibrations are in-plane (A' symmetry) modes. The most active vibration is ν_{21}, followed by ν_{20}, ν_{29}, and ν_{24}. These vibrations are ring deformation modes that generally involve C-C-C bending at the hydrogen-removal site, which is expected to be active given the change in $\theta_{C\text{-}C\text{-}C}$ upon electron detachment. Spectral features X_D and X_L are assigned to the fundamental and combination bands involving ν_{20} and ν_{21}.

We now turn our attention to the series of weak features that extend more than 2000 cm^{-1} below X_A and detailed in Figure 5. These are unlikely to be caused by vibrational hot bands because it would require very high ion internal energies, which are not consistent with the typical outcome of the cryogenic ion trap thermalization. Using the lowest energy peak observed, Peak X_a at 12480 cm^{-1}, as the origin transition for the 2-Tet isomer yields good agreement with the calculated FC spectrum for some of the weaker features in the photoelectron spectrum, as shown in Figure 5. In particular, the positions and relative intensities of peaks X_a-X_c, X_f-X_h, and X_s are in good agreement with this assignment. However, this assignment does not capture the most intense features in this photoelectron spectrum, such as X_d, X_j and X_k. Therefore, we used peak X_d, at 13090 cm^{-1}, as the origin transition for the 1-Tet isomer. This yields an excellent agreement with the calculated FC spectrum for the remaining intense experimental features. Thus, we assign the features in Figure 5 to a mixture of the $\tilde{X}^2A' \leftarrow \tilde{X}^1A'$ transition of the minor 2-Tet and 1-Tet isomers. This assignment yields electron affinities of 1.547±0.002 eV and 1.623±0.002 eV for the

2-Tet and 1-Tet isomers, respectively. These values are in good agreement with the calculated AEA. Again, the FC active vibrations are in-plane (A' symmetry) modes, with the most active modes involving C-C-C bending at the hydrogen-removal site. For 1-Tet, the most active ν_{20}, ν_{18}, and ν_{35} vibrations give rise to the stronger X_k, X_j, and X_n peaks. Other peaks, such as X_q, X_r, and X_t, arise from combination modes involving ν_{20} and ν_{18}. For 2-Tet, the most active ν_{34} vibration gives rise to peak X_f. Complete peak assignments are tabulated in Table 2. Using the relative intensity of peaks X_a, X_d and X_A, as well as the relative intensity of the calculated origin transitions in the FC spectra, we estimate the 12-Tet:1-Tet:2-Tet isomeric population ratio to be 250:2:1.

Finally, we can assign the neutral excited state features in Figure 6A to that of the major 12-Tet isomer. The position of peak A_A yields an adiabatic term energy of 0.952±0.009 eV for the $\tilde{A}^2A$" state, which is consistent with the calculated adiabatic term energy (0.96 eV) of 12-Tet. The corresponding excited-state bands of the 1-Tet and 2-Tet isomers are calculated to lie roughly in the same electron binding energy region. However, given the very small population of these isomers and significant background signal present at this higher photon energy, it would be very difficult to observe them experimentally. As mentioned in section II, the optimized C_s structure for this state has an out-of-plane imaginary frequency. Unfortunately, it was not possible to obtain the lower symmetry structure. Nevertheless, the bottom panel present the FC simulation using the C_s structure and ignoring the imaginary frequency. It predicts very little vibrational activity which is consistent with the observed spectra. However, it doesn't reproduce the feature labeled A_C-A_E. These likely involve 1 or more out-of-plane modes which would become allowed in the lower symmetry structure.

The AEA of the 12-tetracenyl radical determined here is significantly different than the value of 2.6±0.2 eV previously reported by Verlet and co-workers.[19] It is likely that the features

that they identified as arising from direct detachment were in fact also due to the intense indirect detachment signal. While we did not probe the same photon energy range as them, our results displayed in Figure 3F show that at higher photon energy, the direct detachment features are completely obscured by the thermionic emission signal. We also note that the AEA determined here are in-line with the values found for the similar but smaller naphthalenyl and anthracenyl radicals.[17,18]

b) Anion excited state spectrum

Figure 7 shows the total photodetachment yield spectrum in the 16000 – 20000 cm^{-1} region, where distinctly resolved vibrational features can be observed. As discussed above, these non-monotonic increases in photodetachment yield are a clear signature of an anion excited state. The energetic position of these peaks is roughly where the $\tilde{B}^1A'$ anion excited state is predicted. Moreover, the calculated FC spectrum using the optimized TDDFT geometry and vibrational frequencies is in good agreement with the experimental peak positions. However, the predicted vibrational intensities relative to the origin transition are much smaller than what we see in the experiment. Nevertheless, we assign the dominant features, labeled B_A-B_K, to the $\tilde{B}^1A' \leftarrow \tilde{X}^1A'$ transition of 12-Tet. The assignments for these peaks are listed in Table 3.

There are two small peaks, labeled B_a and B_b, which are found below the B_A origin peak. Resonant excitation of these peaks yield photoelectron spectra (Figure 3A and 3B) that show different intensities in the 12000 – 14800 cm^{-1} region, which is associated with the 1-Tet and 2-Tet isomers. Therefore, we assign peaks B_a and B_b to the $\tilde{B}^1A' \leftarrow \tilde{X}^1A'$ origin transitions for the

2-Tet and 1-Tet isomer, respectively. This is consistent with the smaller calculated adiabatic excitation energies in these isomers.

Going back to the $\tilde{B}^1A' \leftarrow \tilde{X}^1A'$ transition of 12-Tet, the discrepancy between the calculated FC intensities and the observed spectrum may be attributable to three different causes. First, it is conceivable that the relatively low-level TDDFT calculations underestimate the geometry changes upon excitation. Unfortunately, geometry optimization using higher level of theory, such as equation-of-motion coupled clusters (EOM-CCSD), would be challenging given the size and low symmetry of the tetracenyl anion. Secondly, we note that using photoelectron yield as an indirect measurement of the anion absorption spectrum can lead to some distortions in the observed intensity compared to the absorption cross-section. This is because the co-linear arrangement of our SEVI setup limits our observation of photoelectrons to those produced in the ~500 ns immediately following laser excitation. Therefore, if the rate of autodetachment of a particular vibrational state is higher than another, it would then appear much more intensely in our total photodetachment yield spectrum. Finally, we note that there may be additional anion excited states whose broad features are contributing to the overall photoelectron intensities observed between 17000 cm^{-1} and 22000 cm^{-1} (Figure 2). Exploratory TDDFT calculations found 3 other excited states in this energy range, although they are all predicted to have low absorption cross-section ($f < 0.001$). However, higher level computations will be necessary to confidently assign any of the broader features shown in Figure 2.

The vibrationally resolved features in Figure 7 have FWHM of about 30-50 cm^{-1}, which would correspond to a lifetime of at least 100fs for these vibrational states. This long lifetime with respect to autodetachment is consistent with the nature of the electronic configuration of this excited state. The main character of the $\tilde{B}^1A'$ state involves the excitation of a HOMO-1 electron

in to the LUMO. Autodetachment from this electronic configuration cannot directly yield the neutral ground-state. The lowest energy neutral state that can be produce by autodetachment is the $^2A''$ neutral excited-state which lies ~5000 cm^{-1} above this anion excited state. Therefore, it is not too surprising that the $\tilde{B}^1A'$ anion state is relatively stable with respect to autodetachment. This is also consistent with the observed photoelectron spectra resulting from the excitation to this anion excited state (for example, see Figure 3D-F). Specifically, the produced photoelectrons have a kinetic energy distribution peaking near eKE = 0, meaning that thermionic emission is the main pathway for electron detachment.[41–43] This implies that the main relaxation pathway for the $\tilde{B}^1A'$ state is not autodetachment, but internal conversion to a vibrationally hot ground-state followed by thermionic emission. Such a long lifetime for this anion excited state can have implications for the formation of anions in interstellar medium. If the excited anion can be created efficiently by an electron attachment process, its lifetime might allow for fluorescence to quench the excess internal energy and efficiently produce a stable tetracenyl anion.

V. Conclusion

In this work, we studied the tetracenyl anion and neutral radical using high-resolution photoelectron spectroscopy of cryogenic anions. The systematic mapping of photodetachment yield as a function photon energy reveals a rich manifold of intense bands corresponding to the excitation of valence anion excited states located above the detachment threshold. The lifetime of one of these states is long enough to produce vibrationally resolved spectrum. However, these resonant excitation processes produce photoelectrons that can severely interfere and even completely obscure the direct photodetachment signal. Careful selection of the photon energies is necessary in order to measure photoelectron spectra which are meaningful for studying the

corresponding neutral radical states. Using this approach, as well as FC simulations of the vibrationally resolved photoelectron spectra, we provide a corrected value for the electron affinity of the 12-Tet isomer and new values for the 1-Tet and 2-Tet isomers. Finally, we note that the interferences from anion resonances observed here are likely to be present to some extent in the photoelectron spectroscopy of most PAHs and related species. The systematic measurement of the photodetachment yield provides a generally applicable scheme for selection of proper photodetachment wavelengths. It also provides a powerful tool for the experimental vibronic characterization of such anion resonances.

Acknowledgements

This work was supported by the U.S. Department of Energy, Office of Science, Basic Energy Sciences, under award No. DE-SC0018902. The computational resources used in this work are supported by National Science Foundation Grant CHE-0840494.

References

(1) Page, V. L.; Snow, T. P.; Bierbaum, V. M. Hydrogenation and Charge States of Polycyclic Aromatic Hydrocarbons in Diffuse Clouds. II. Results. *Astrophys. J.* **2003**, *584* (1), 316. https://doi.org/10.1086/345595.

(2) Kaiser, R. I.; Hansen, N. An Aromatic Universe–A Physical Chemistry Perspective. *J. Phys. Chem. A* **2021**, *125* (18), 3826–3840. https://doi.org/10.1021/acs.jpca.1c00606.

(3) Malloci, G.; Mulas, G.; Cecchi-Pestellini, C.; Joblin, C. Dehydrogenated Polycyclic Aromatic Hydrocarbons and UV Bump. *Astron. Astrophys.* **2008**, *489* (3), 1183–1187. https://doi.org/10.1051/0004-6361:200810177.

(4) Duley, W. W. Polycyclic Aromatic Hydrocarbons, Carbon Nanoparticles and the Diffuse Interstellar Bands. *Faraday Discuss.* **2006**, *133* (0), 415–425. https://doi.org/10.1039/B516323D.

(5) Kaiser, R. I.; Parker, D. S. N.; Mebel, A. M. Reaction Dynamics in Astrochemistry: Low-Temperature Pathways to Polycyclic Aromatic Hydrocarbons in the Interstellar Medium. *Annu. Rev. Phys. Chem.* **2015**, *66* (1), 43–67. https://doi.org/10.1146/annurev-physchem-040214-121502.

(6) Parker, D. S. N.; Zhang, F.; Kim, Y. S.; Kaiser, R. I.; Landera, A.; Kislov, V. V.; Mebel, A. M.; Tielens, A. G. G. M. Low Temperature Formation of Naphthalene and Its Role in the Synthesis of PAHs (Polycyclic Aromatic Hydrocarbons) in the Interstellar Medium. *Proc. Natl. Acad. Sci.* **2012**, *109* (1), 53–58. https://doi.org/10.1073/pnas.1113827108.

(7) Herbst, E. Can Negative Molecular Ions Be Detected in Dense Interstellar Clouds? *Nature* **1981**, *289* (5799), 656–657. https://doi.org/10.1038/289656a0.

(8) Herbst, E.; Osamura, Y. Calculations on the Formation Rates and Mechanisms for CnH Anions in Interstellar and Circumstellar Media. *Astrophys. J.* **2008**, *679* (2), 1670. https://doi.org/10.1086/587803.

(9) Wakelam, V.; Herbst, E. Polycyclic Aromatic Hydrocarbons in Dense Cloud Chemistry. *Astrophys. J.* **2008**, *680* (1), 371–383. https://doi.org/10.1086/587734.

(10) Garcia-Sanz, A.; Carelli, F.; Sebastianelli, F.; Gianturco, F. A.; Garcia, G. Dynamics of Formation of Anthracene Anions in Molecular Clouds and Protoplanetary Atmospheres. *New J. Phys.* **2013**, *15* (1), 013018. https://doi.org/10.1088/1367-2630/15/1/013018.

(11) Osterwalder, A.; Nee, M. J.; Zhou, J.; Neumark, D. M. High Resolution Photodetachment Spectroscopy of Negative Ions via Slow Photoelectron Imaging. *J. Chem. Phys.* **2004**, *121* (13), 6317–6322. https://doi.org/10.1063/1.1787491.

(12) Neumark, D. M. Slow Electron Velocity-Map Imaging of Negative Ions: Applications to Spectroscopy and Dynamics. *J. Phys. Chem. A* **2008**, *112* (51), 13287–13301. https://doi.org/10.1021/jp807182q.

(13) Weichman, M. L.; Neumark, D. M. Slow Photoelectron Velocity-Map Imaging of Cryogenically Cooled Anions. *Annu. Rev. Phys. Chem.* **2018**, *69* (1), 101–124. https://doi.org/10.1146/annurev-physchem-050317-020808.

(14) Wang, X.-B.; Wang, L.-S. Development of a Low-Temperature Photoelectron Spectroscopy Instrument Using an Electrospray Ion Source and a Cryogenically Controlled Ion Trap. *Rev. Sci. Instrum.* **2008**, *79* (7), 073108. https://doi.org/10.1063/1.2957610.

(15) Boyarkin, O. V.; Mercier, S. R.; Kamariotis, A.; Rizzo, T. R. Electronic Spectroscopy of Cold, Protonated Tryptophan and Tyrosine. *J. Am. Chem. Soc.* **2006**, *128* (9), 2816–2817. https://doi.org/10.1021/ja058383u.

(16) Wolk, A. B.; Leavitt, C. M.; Garand, E.; Johnson, M. A. Cryogenic Ion Chemistry and Spectroscopy. *Acc. Chem. Res.* **2014**, *47* (1), 202–210. https://doi.org/10.1021/ar400125a.

(17) Weichman, M. L.; Kim, J. B.; DeVine, J. A.; Levine, D. S.; Neumark, D. M. Vibrational and Electronic Structure of the Alpha- and Beta-Naphthyl Radicals via Slow

Photoelectron Velocity-Map Imaging. *J Am Chem Soc* **2015**, *137* (4), 1420–1423. https://doi.org/10.1021/ja5124896.

(18) Weichman, M. L.; DeVine, J. A.; Levine, D. S.; Kim, J. B.; Neumark, D. M. Isomer-Specific Vibronic Structure of the 9-, 1-, and 2-Anthracenyl Radicals via Slow Photoelectron Velocity-Map Imaging. *Proc. Natl. Acad. Sci.* **2016**, *113* (7), 1698–1705. https://doi.org/10.1073/pnas.1520862113.

(19) Bull, J. N.; West, C. W.; Verlet, J. R. R. Internal Conversion Outcompetes Autodetachment from Resonances in the Deprotonated Tetracene Anion Continuum. *Phys. Chem. Chem. Phys.* **2015**, *17* (48), 32464–32471. https://doi.org/10.1039/C5CP05388A.

(20) Jordan, K. D.; Burrow, P. D. Temporary Anion States of Polyatomic Hydrocarbons. *Chem. Rev.* **1987**, *87* (3), 557–588. https://doi.org/10.1021/cr00079a005.

(21) Burrow, P. D.; Michejda, J. A.; Jordan, K. D. Electron Transmission Study of the Temporary Negative Ion States of Selected Benzenoid and Conjugated Aromatic Hydrocarbons. *J. Chem. Phys.* **1987**, *86* (1), 9–24. https://doi.org/10.1063/1.452598.

(22) Anstöter, C. S.; Bull, J. N.; Verlet, J. R. R. Ultrafast Dynamics of Temporary Anions Probed through the Prism of Photodetachment. *Int. Rev. Phys. Chem.* **2016**, *35* (4), 509–538. https://doi.org/10.1080/0144235X.2016.1203522.

(23) Stanley, L. H.; Anstoter, C. S.; Verlet, J. R. R. Resonances of the Anthracenyl Anion Probed by Frequency-Resolved Photoelectron Imaging of Collision-Induced Dissociated Anthracene Carboxylic Acid. *Chem. Sci.* **2017**, *8* (4), 3054–3061. https://doi.org/10.1039/c6sc05405f.

(24) West, C. W.; Bull, J. N.; Antonkov, E.; Verlet, J. R. R. Anion Resonances of Para-Benzoquinone Probed by Frequency-Resolved Photoelectron Imaging. *J. Phys. Chem. A* **2014**, *118* (48), 11346–11354. https://doi.org/10.1021/jp509102p.

(25) Mensa-Bonsu, G.; Lietard, A.; Tozer, D. J.; Verlet, J. R. R. Low Energy Electron Impact Resonances of Anthracene Probed by 2D Photoelectron Imaging of Its Radical Anion. *J. Chem. Phys.* **2020**, *152* (17), 174303. https://doi.org/10.1063/5.0007470.

(26) Kim, J. H.; Lee, S. H.; Song, J. K. Photoelectron Spectroscopy of Pyrene Anion Clusters: Autodetachment via Excited States of Anion and Intermolecular Interactions in Anion Clusters. *J. Chem. Phys.* **2009**, *130* (12), 124321. https://doi.org/10.1063/1.3093032.

(27) Ashworth, E. K.; Anstöter, C. S.; Verlet, J. R. R.; Bull, J. N. Autodetachment Dynamics of 2-Naphthoxide and Implications for Astrophysical Anion Abundance. *Phys. Chem. Chem. Phys.* **2021**, *23* (10), 5817–5823. https://doi.org/10.1039/D1CP00261A.

(28) Henley, A.; Fielding, H. H. Anion Photoelectron Spectroscopy of Protein Chromophores. *Int. Rev. Phys. Chem.* **2019**, *38* (1), 1–34. https://doi.org/10.1080/0144235X.2018.1548807.

(29) Patel, A. M.; Henley, A.; Parkes, M. A.; Assmann, M.; Worth, G. A.; Anderson, J. C.; Fielding, H. H. Shining Light on the Electronic Structure and Relaxation Dynamics of the Isolated Oxyluciferin Anion. *Phys. Chem. Chem. Phys.* **2020**, *22* (34), 19022–19032. https://doi.org/10.1039/D0CP03276J.

(30) Kregel, S. J.; Thurston, G. K.; Zhou, J.; Garand, E. A Multi-Plate Velocity-Map Imaging Design for High-Resolution Photoelectron Spectroscopy. *J. Chem. Phys.* **2017**, *147* (9), 094201. https://doi.org/10.1063/1.4996011.

(31) Gascooke, J. R.; Gibson, S. T.; Lawrance, W. D. A "Circularisation" Method to Repair Deformations and Determine the Centre of Velocity Map Images. *J. Chem. Phys.* **2017**, *147* (1), 013924. https://doi.org/10.1063/1.4981024.

(32) Hansen, E. W.; Law, P.-L. Recursive Methods for Computing the Abel Transform and Its Inverse. *JOSA A* **1985**, *2* (4), 510–520. https://doi.org/10.1364/JOSAA.2.000510.

(33) Weigend, F.; Ahlrichs, R. Balanced Basis Sets of Split Valence, Triple Zeta Valence and Quadruple Zeta Valence Quality for H to Rn: Design and Assessment of Accuracy. *Phys. Chem. Chem. Phys.* **2005**, *7* (18), 3297–3305. https://doi.org/10.1039/B508541A.

(34) Rappoport, D.; Furche, F. Property-Optimized Gaussian Basis Sets for Molecular Response Calculations. *J. Chem. Phys.* **2010**, *133* (13), 134105. https://doi.org/10.1063/1.3484283.

(35) Frisch, M. J.; Trucks, G. W.; Schlegel, H. B.; Scuseria, G. E.; Robb, M. A.; Cheeseman, J. R.; Scalmani, G.; Barone, V.; Petersson, G. A.; Nakatsuji, H.; et al. *Gaussian 16 Rev. C.01*; Wallingford, CT, 2016.

(36) Papas, B. N.; Wang, S.; DeYonker, N. J.; Woodcock, H. L.; Schaefer, H. F. Naphthalenyl, Anthracenyl, Tetracenyl, and Pentacenyl Radicals and Their Anions. *J. Phys. Chem. A* **2003**, *107* (32), 6311–6316. https://doi.org/10.1021/jp030494x.

(37) Gozem, S.; Krylov, A. I. The EzSpectra Suite: An Easy-to-Use Toolkit for Spectroscopy Modeling. *WIREs Comput. Mol. Sci.* **2021**, e1546. https://doi.org/10.1002/wcms.1546.

(38) Theis, M. L.; Candian, A.; Tielens, A. G. G. M.; Lee, T. J.; Fortenberry, R. C. Electronically Excited States of Anisotropically Extended Singly-Deprotonated PAH Anions. *J. Phys. Chem. A* **2015**, *119* (52), 13048–13054. https://doi.org/10.1021/acs.jpca.5b10421.

(39) Wigner, E. P. On the Behavior of Cross Sections Near Thresholds. *Phys. Rev.* **1948**, *73* (9), 1002–1009. https://doi.org/10.1103/PhysRev.73.1002.

(40) Khatymov, R. V.; Tuktarov, R. F.; Muftakhov, M. V. Lifetime of Negative Molecular Ions of Tetracene and Pentacene with Respect to the Autodetachment of an Electron. *JETP Lett.* **2011**, *93* (8), 437–441. https://doi.org/10.1134/S002136401108011X.

(41) Campbell, E. E. B.; Levine, R. D. Delayed Ionization and Fragmentation En Route to Thermionic Emission: Statistics and Dynamics. *Annu. Rev. Phys. Chem.* **2000**, *51* (1), 65–98. https://doi.org/10.1146/annurev.physchem.51.1.65.

(42) Andersen, J. U.; Bonderup, E.; Hansen, K. Thermionic Emission from Clusters. *J. Phys. B At. Mol. Opt. Phys.* **2002**, *35* (5), R1. https://doi.org/10.1088/0953-4075/35/5/201.

(43) Adams, C. L.; Hansen, K.; Weber, J. M. Vibrational Autodetachment from Anionic Nitroalkane Chains: From Molecular Signatures to Thermionic Emission. *J. Phys. Chem. A* **2019**, *123* (40), 8562–8570. https://doi.org/10.1021/acs.jpca.9b07780.

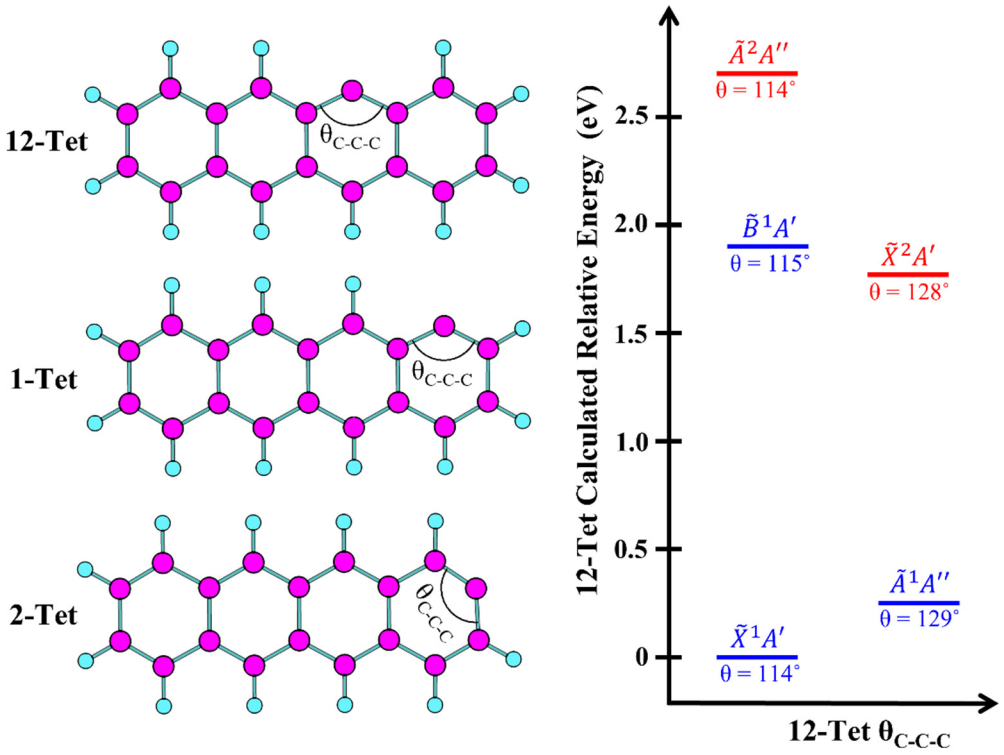

Figure 1. (Left) Geometries of the three tetracenyl isomers. 12-Tet corresponds to the removal of H12; 1-Tet corresponds to the removal of H1; 2-Tet corresponds to the removal of H2. (Right) Relative energies of anion (blue) and neutral (red) ground and excited states in the 12-Tet isomer. The states are offset in the x-axis by their calculated $\theta_{C\text{-}C\text{-}C}$ angles.

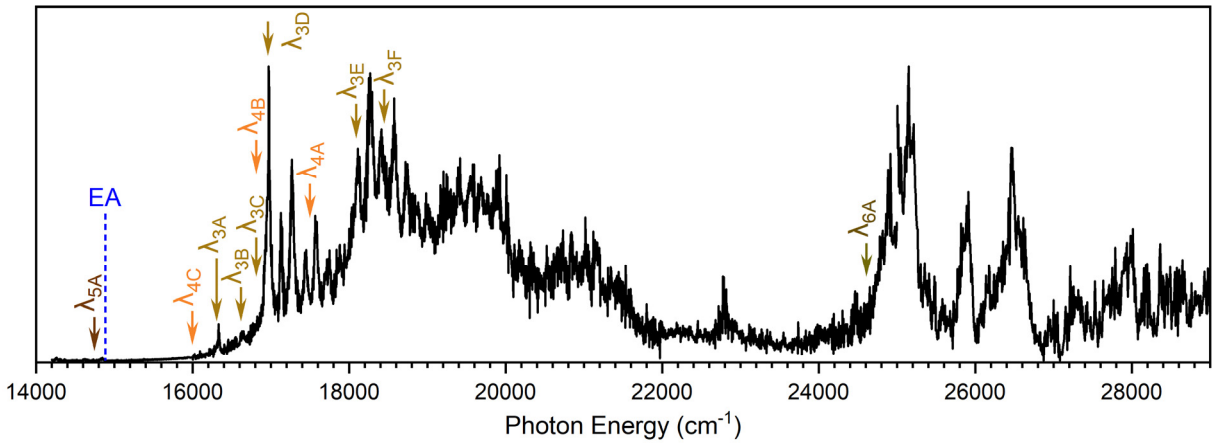

Figure 2. Total photodetachment cross-section spectrum in the 14000 – 29000 cm^{-1} range. The experimental electron affinity (EA) is determined more precisely in Figure 4, but its position is marked here for reference. Photon energies corresponding to photoelectron spectra shown in Figures 3 (yellow), Figure 4 (green), Figure 5 (red) and Figure 6 (purple) are indicated by labeled arrows.

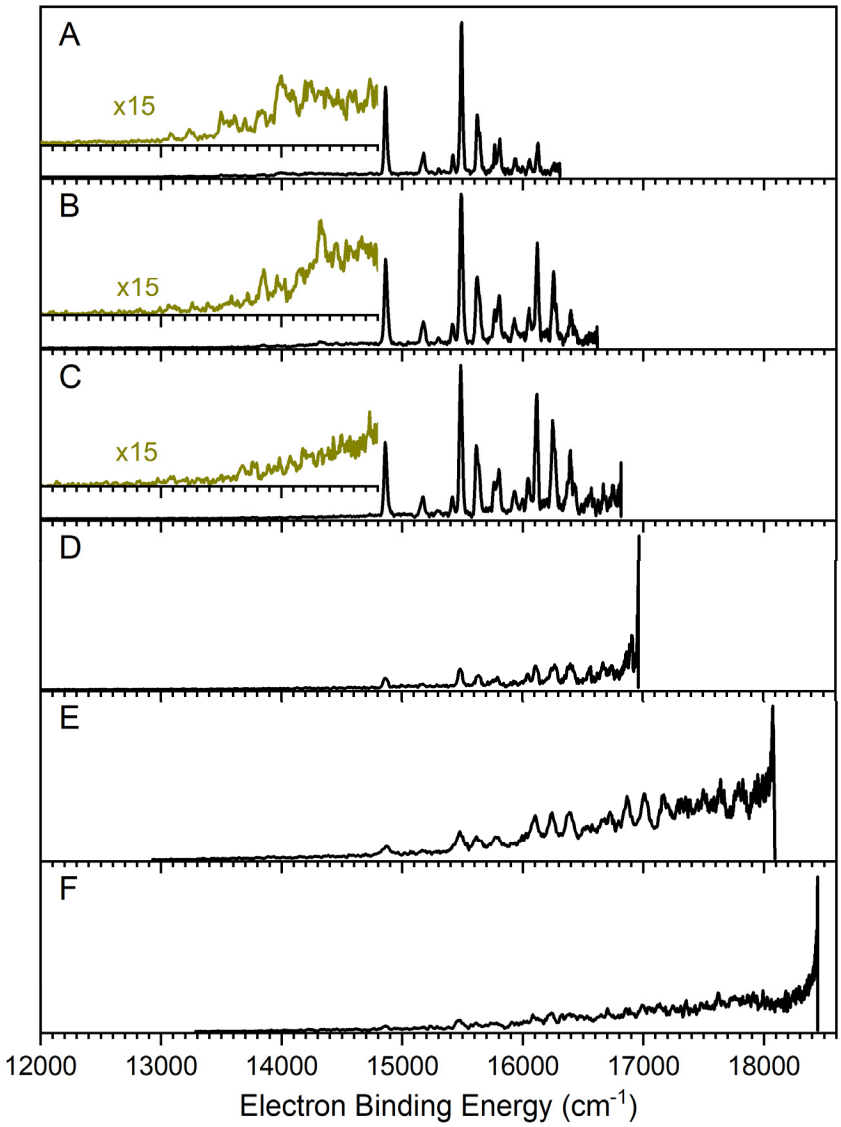

Figure 3. Photoelectron spectra acquired with photon energies of 16370 cm^{-1} (A), 16617 cm^{-1} (B), 16815 cm^{-1} (C), 16964 cm^{-1} (D), 18090 cm^{-1} (E), and 18447 cm^{-1} (F). Insert spectra in panels A-C show ×15 view in the 12000-14800 cm^{-1} region: λ_{3A} and λ_{3B} are resonant with weak features in the photodetachment cross-section spectrum while λ_{3C} is not (see Figure 2), which result in different intensities in the 12000-14800 cm^{-1} region in these three spectra.

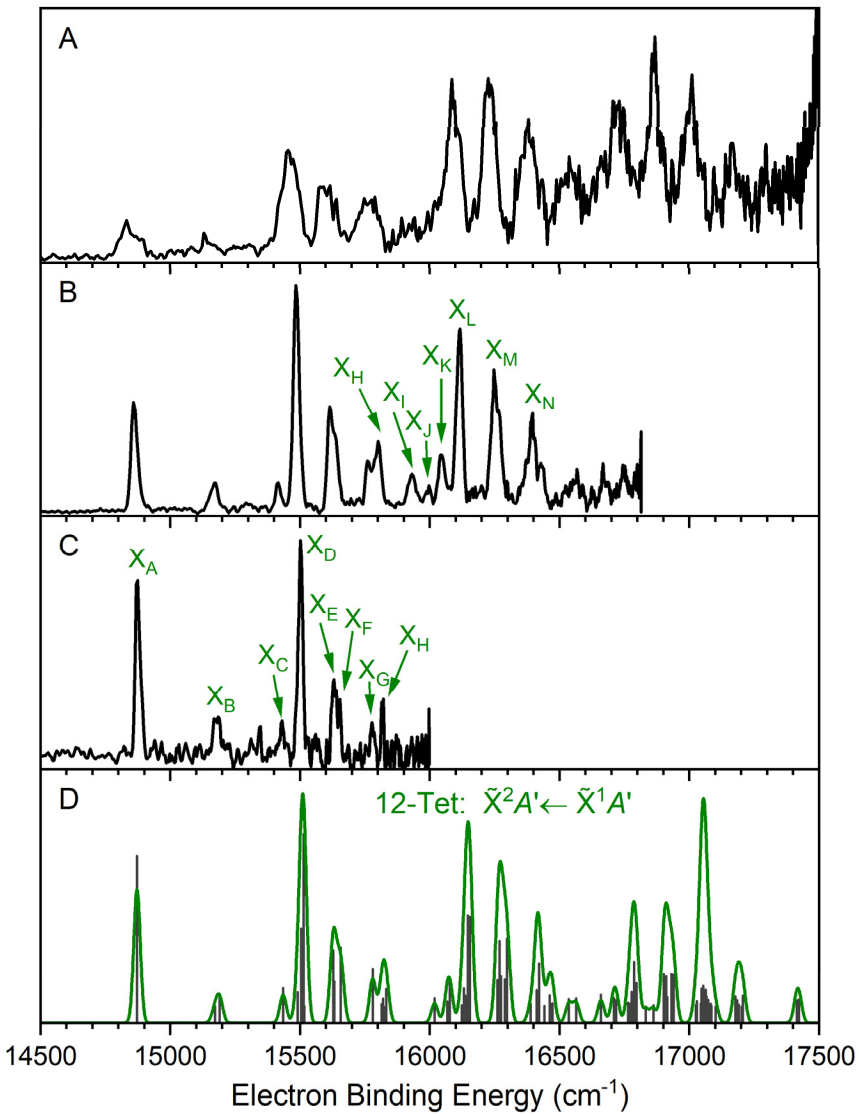

Figure 4. Photoelectron spectra acquired with photon energies of 17500 cm^{-1} (A), 16815 cm^{-1} (B), and 15998 cm^{-1} (C). Assignments are made by comparisons to the calculated Franck-Condon spectrum of the $\tilde{X}^2A' \leftarrow \tilde{X}^1A'$ transition of the 12-Tet isomer (D), where the origin transition is aligned to peak X_A.

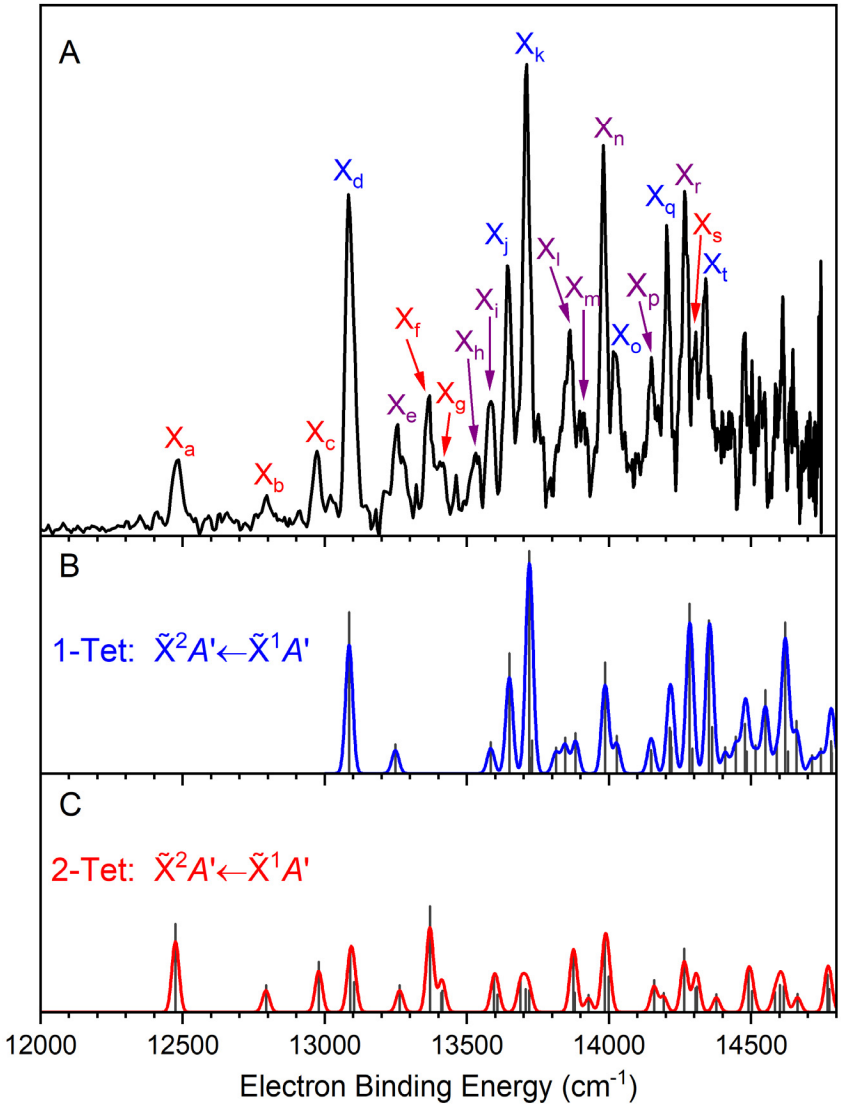

Figure 5. (A) Photoelectron spectrum acquired with photon energies of 14747 cm^{-1}. The peak label color corresponds to contribution from the 1-Tet isomer (blue), 2-Tet isomer (red) or both (purple) (B) Calculated Franck-Condon spectrum of the $\tilde{X}^2A' \leftarrow \tilde{X}^1A'$ transition of the 1-Tet isomer, where the origin transition is aligned to peak X_d. (C) Calculated Franck-Condon spectrum of the $\tilde{X}^2A' \leftarrow \tilde{X}^1A'$ transition of the 2-Tet isomer, where the origin transition is aligned to peak X_a.

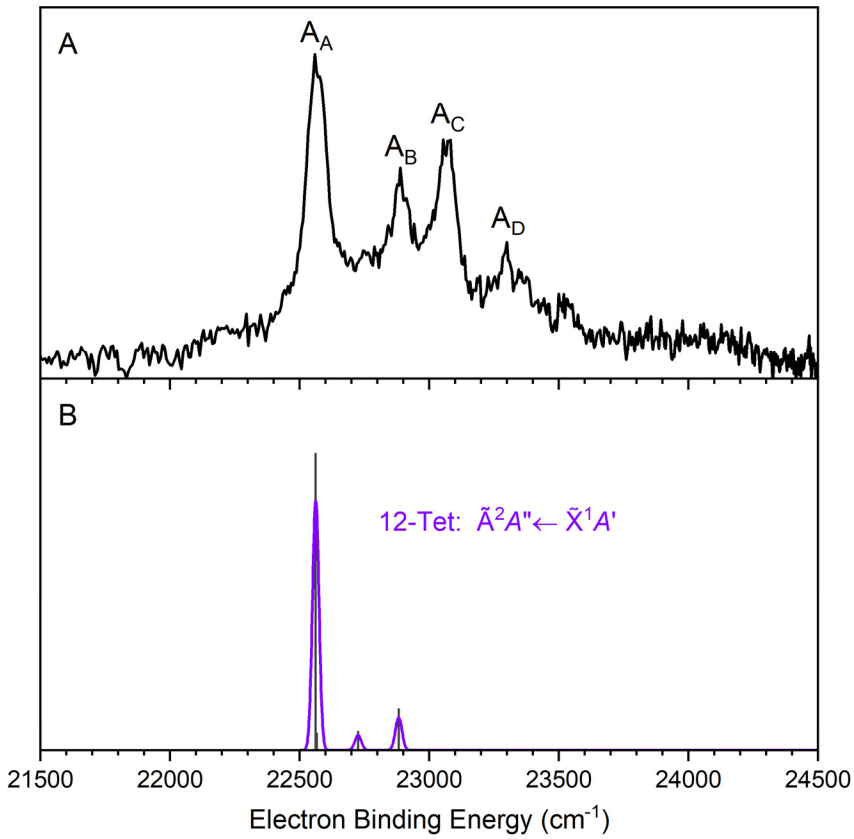

Figure 6. (A) Photoelectron spectrum acquired with photon energies of 24610 cm^{-1}. (B) Calculated Franck-Condon spectrum of the $\tilde{A}^2A'' \leftarrow \tilde{X}^1A'$ transition of the 12-Tet isomer, where the origin transition is aligned to peak A_A.

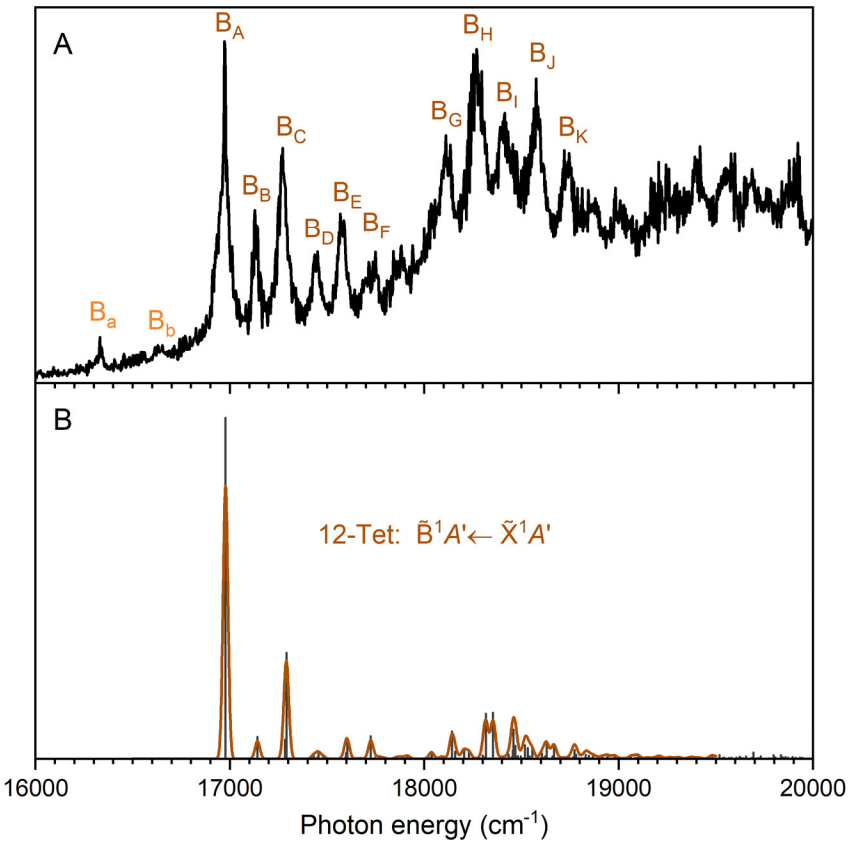

Figure 7. (A) Total photodetachment cross-section spectrum in the 16000 – 20000 cm^{-1} range. (B) Calculated Franck-Condon spectrum of the $\tilde{B}^1A' \leftarrow \tilde{X}^1A'$ transition of the 12-Tet isomer, where the origin transition is aligned to peak B_A.

Table 1. Experimental peak positions (eBE) and assignments for the $\tilde{X}^2A' \leftarrow \tilde{X}^1A'$ transition (shown in Figure 4) and $\tilde{A}^2A'' \leftarrow \tilde{X}^1A'$ transition (shown in Figure 6) of the 12-Tet isomer. All values are in cm^{-1}. The uncertainty on the eBE corresponds to a peak's half-width at half maximum. Where there are multiple assignments for a single observed peak, the more dominant transition(s) are bolded.

Peak	eBE	Exp. Vib. Freq.	Assignment	Calc. Vib. Freq.
X_A	14887(4)	-	0-0 ($\tilde{X}^2A' \leftarrow \tilde{X}^1A'$)	14250
X_B	15179(17)	293	**ν7(A') in-plane ring deform.**; **ν9(A') in-plane ring deform.**	**300**; **319**
X_C	15431(9)	544	ν17(A') in-plane ring deform.	563
X_D	15502(10)	613	ν19(A') in-plane ring deform.; **ν20(A') in-plane ring deform.**; **ν21(A') in-plane ring deform.**	*619*; **632**; **642**
X_E	15630(9)	743	**ν24(A') in-plane ring str.**; **ν26(A') in-plane ring str.**	**756**; **761**
X_F	15653(9)	766	ν29(A') in-plane ring deform.	785
X_G	15780(18)	893	ν34(A') in-plane ring deform.	908
X_H	15820(14)	933	**ν7 + ν21**; **ν37(A') in-plane ring deform.**; **ν9 + ν20**; **ν9 + ν21**	**942**; **949**; **951**; **961**
X_I	15932(17)	1044		
X_J	15991(16)	1104	ν44(A') in-plane CH bend	1147
X_K	16048(28)	1161	**ν17 + ν20**; **ν17 + ν21**	**1195**; **1205**
X_L	16114(15)	1227	ν19 + ν20; ν19 + ν21; 2ν20; **ν20 + ν21**; ν52(A') in-plane CH bend + ring deform.; **2ν21**	1251; 1261; 1264; **1274**; 1279; **1284**
X_M	16249(15)	1362	ν20 + ν24; ν20 + ν26; **ν21 + ν24**; ν21 + ν26	1388; 1393; **1398**; 1403
	16272(15)	1385	ν20 + ν29; **ν21 + ν29**	1417; **1427**
X_N	16393(24)	1506	ν24 + ν26; ν20 + ν34; ν24 + ν29; ν26 + ν29; **ν21 + ν34**	1517; 1540; 1541; 1546; **1550**
	16433(25)	1546	**2ν29**; **ν21 + ν37**; **ν9 + ν20 + ν21**; **ν9 + 2ν21**	**1570**; **1591**; **1593**; **1603**
A_A	22570(68)	-	**0-0 ($\tilde{A}^2A'' \leftarrow \tilde{X}^1A'$)**	21996
A_B	22880(68)	310	ν9(A') in-plane ring deform.	320
A_C	23070(68)	500		
A_D	23300(68)	730		

Table 2. Experimental peak positions (eBE) and assignments for the $\tilde{X}^2A' \leftarrow \tilde{X}^1A'$ transition of the 1-Tet and 2-Tet isomers (shown in Figure 5). All values are in cm^{-1}. The uncertainty on the eBE corresponds to a peak's half-width at half maximum. Where there are multiple assignments for a single observed peak, the more dominant transition(s) are bolded.

Peak	eBE	Exp. Vib. Freq.	Isomer	Assignment	Calc. Vib. Freq.
X_a	12481(20)	-	2-Tet	0-0 ($\tilde{X}^2A' \leftarrow \tilde{X}^1A'$)	12347
X_b	12795(15)	314	2-Tet	ν8(A') in-plane ring deform.	319
X_c	12972(15)	491	2-Tet	ν15(A') in-plane ring deform.	504
X_d	13088 (18)	607	2-Tet	ν19(A') in-plane ring deform.; ν20(A') in-plane ring deform.	616; 629
		-	1-Tet	**0-0 ($\tilde{X}^2A' \leftarrow \tilde{X}^1A'$)**	**12678**
X_e	13260(28)	779	2-Tet	ν29(A') in-plane ring deform.	789
		172	1-Tet	**ν4(A') in-plane ring deform.**	**163**
X_f	13365(14)	884	2-Tet	ν34(A') in-plane ring deform.	895
X_g	13407(19)	926	2-Tet	**ν8 + ν19**; **ν38(A') in-plane ring deform.**	**935**; **940**
X_h	13530(18)	1049 or 442			
X_i	13583(16)	1102	2-Tet	**ν15 + ν19**; ν15 + ν20	**1120**; 1133
		495	1-Tet	**ν15(A') in-plane ring deform.**	**498**
X_j	13646(16)	558	1-Tet	ν18(A') in-plane ring deform.	564
X_k	13710(16)	622	1-Tet	**ν20(A') in-plane ring deform.**; ν21(A') in-plane ring deform.	**633**; 643
X_l	13858(24)	1377	2-Tet	**ν15 + ν34**; ν19 + ν29	**1399**; 1404
		770	1-Tet	**ν25(A') in-plane ring str.**	**760**
X_m	13910(13)	1429	2-Tet	ν17 + ν34	1453
		822	1-Tet	**ν4 + ν20**	**796**
X_n	13981(12)	1500	2-Tet	ν19 + ν34; ν20 + ν34	1511; 1524
		893	1-Tet	**ν35(A') in-plane ring deform.**	**901**
X_o	14024(17)	936	1-Tet	ν38(A') in-plane ring deform.	941
X_p	14152(19)	1671	2-Tet	ν29 + ν34	1684
		1064	1-Tet	**ν15 + ν18**; **ν4 + ν35**	**1062**; **1064**
X_q	14205(12)	1117	1-Tet	**2ν18**; **ν15 + ν20**; ν44(A') in-plane CH bend + ring deform.	**1128**; **1131**; 1134
X_r	14268(12)	1787	2-Tet	2ν34	1790
		1180	1-Tet	**ν18 + ν20**; ν18 + ν21	**1197**; 1207
X_s	14303(16)	1822	2-Tet	**ν8 + ν19 + ν34**; **ν34 + ν38**	**1830**; **1835**
X_t	14338(15)	1250	1-Tet	**2ν20**; ν20 + ν21	**1266**; 1276

Table 3. Experimental peak positions (eBE) and assignments for the $\tilde{B}^1A' \leftarrow \tilde{X}^1A'$ transition of the 12-Tet (shown in Figure 7). All values are in cm^{-1} The uncertainty on the eBE corresponds to a peak's half-width at half maximum. Where there are multiple assignments for a single observed peak, the more dominant transition(s) are bolded.

Peak	eBE	Exp. Vib. Freq.	Assignment	Calc. Vib. Freq.
B_A	16972(28)		0-0 ($\tilde{B}^1A' \leftarrow \tilde{X}^1A'$)	15350
B_B	17133(16)	161	ν4(A') in-plane ring deform.	164
B_C	17271(28)	299	ν7(A') in-plane ring deform.; **ν8(A') in-plane ring deform.**	306; **314**
B_D	17444(27)	472	**ν13(A') in-plane ring deform.**; **ν4 + ν8**; ν15(A') in-plane ring deform.	**454**; **478**; 501
B_E	17576(26)	604	ν7 + ν8; **2ν8**	620; **628**
B_F	17734(64)	762	ν25(A') in-plane ring str.	747
B_G	18102(67)	1130	**ν47(A') in-plane CH bend**; ν48(A') in-plane CH bend + ring deform.	**1165**; 1182
B_H	18269(44)	1297	ν56(A') in-plane ring str.; **ν57(A') in-plane ring str.**; **ν59(A') in-plane ring str.**	1323; **1339**; **1376**

TOC Graphic

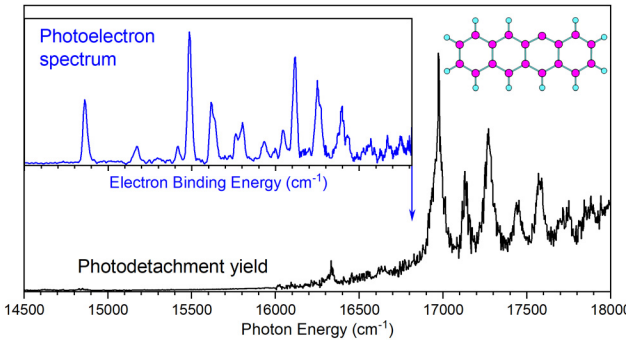
Photoelectron
spectrum
Electron Binding Energy (cm-1)
Photodetachment yield
14500
15000
15500
16000
16500
17000
17500
Photon Energy (cm-1)